Journal of *Marine Science and Engineering*

MDPI

Article

Multiphase-Thermal Flow Simulation in a Straight Vacuum-Insulated LH_2 Pipe: Fuel Gas Supply System in a LH_2-Fueled Ship

Yong-Seok Seo, Soh-Myung Chung and Jong-Chun Park *

Department of Naval Architecture and Ocean Engineering, Pusan National University, Busan 46241, Republic of Korea; yongseok40@pusan.ac.kr (Y.-S.S.); smchung@pusan.ac.kr (S.-M.C.)
* Correspondence: jcpark@pnu.edu

Abstract: Hydrogen, stored as a liquid at cryogenic temperatures to enhance transport efficiency, is susceptible to boiling due to thermal fluctuations, underscoring the importance of investigating thermal insulation for liquid hydrogen piping. Evaluating their suitability and effectiveness for hydrogen ship piping remains critical. This study conducted numerical simulations to analyze insulation and phase-change impacts on the multiphase thermal flow of piping systems used for the Fuel Gas Supply System (FGSS) of hydrogen-fueled ships. The accuracy of the adopted phase-change model was validated against selected experimental cases of boiling phenomena, demonstrating agreement with experimental results. We applied the validated phase-change model to simulate multiphase thermal flow in an LH_2 pipe and evaluated the thermal performance of insulation materials. The insulation material considered in this study is a composite insulation system with various filling materials. Specifically, we observed that the insulation performance was superior when utilizing a combination of vacuum insulation along with MLI Mylar nets. Additionally, we evaluated the safety within the pipe by comparing the amount of vapor generated inside with the Lower Flammability Limit (LFL). Our results indicate that a safety assessment of the insulation is necessary when no filling material is used. Quantitatively, we found that pipes with composite vacuum and MLI Mylar net insulation reduced vapor generation by 45% compared to vacuum-only insulation, highlighting the effectiveness of the proposed insulation method.

Keywords: liquid hydrogen (LH_2); wall boiling model; pipe flow; fuel gas supply system (FGSS); multiphase thermal flow; lower flammability limit (LFL)

check for updates

Citation: Seo, Y.-S.; Chung, S.-M.; Park, J.-C. Multiphase-Thermal Flow Simulation in a Straight Vacuum-Insulated LH_2 Pipe: Fuel Gas Supply System in a LH_2-Fueled Ship. *J. Mar. Sci. Eng.* **2024**, *12*, 914. https://doi.org/10.3390/jmse12060914

Academic Editor: Atilla Incecik

Received: 7 April 2024
Revised: 20 May 2024
Accepted: 28 May 2024
Published: 30 May 2024

Copyright: © 2024 by the authors. Licensee MDPI, Basel, Switzerland. This article is an open access article distributed under the terms and conditions of the Creative Commons Attribution (CC BY) license (https://creativecommons.org/licenses/by/4.0/).

1. Introduction

The globalization-driven surge in international trade has heightened the reliance on transportation, which predominantly uses fossil fuels, thereby contributing significantly to greenhouse gas emissions [1]. Notably, the total GHG emissions—including carbon dioxide, methane, and nitrous oxide, expressed in CO_2e—of shipping have increased from 977 million tons in 2012 to 1076 million tons in 2018 (9.6% increase) [2,3]. Consequently, addressing the increase in greenhouse gases, which leads to climate change, ocean acidification, and biodiversity loss, has become imperative.

The International Chamber of Shipping (ICS) reports that sea transport handles about 90% of global trade, underlining the escalating importance of maritime shipping and the urgent need to minimize emissions from this sector [4]. The International Maritime Organization (IMO) has aimed for net-zero CO_2 emissions by 2050, highlighting the potential role of hydrogen as a sustainable fuel alternative [5,6]. Hydrogen is non-toxic and disperses rapidly due to its lighter-than-air nature, making it safer than other fuels in the case of a leak. However, when gaseous hydrogen accumulates in an enclosed space, it poses an explosion risk because of its low ignition energy [7]. The flammability limit of gaseous hydrogen ranges from 4 to 75%, the explosion limit from 18.3 to 59%, and its minimum

ignition energy is 0.02 mJ [8]. Therefore, designing a safe hydrogen system that considers the unique properties of hydrogen is crucial for ensuring the safe storage and transportation of hydrogen.

Notable examples of hydrogen-powered ships include the US Sandia Lab's technical review of the SF-BREEZE [9], Germany's development of the FCS Alsterwasser [10], and Norway's construction plans for the Viking Cruise hydrogen-fueled ship [11].

For the development of hydrogen-powered ships, it is essential to concurrently advance specific component technologies and overall ship systems [12]. In the Fuel Gas Supply System (FGSS) of hydrogen-fueled ships, analyzing thermofluid dynamics in pipes carrying cryogenic liquids necessitates careful consideration of boiling and insulation phenomena. When cryogenic liquids flow through pipes, the temperature disparity between the pipe wall and the liquid triggers boiling, resulting in the generation of boil-off gas (BOG) or vapor. An increase in BOG volume can alter the pressure inside the pipes, potentially compromising safety. Addressing the issues related to the transportation of cryogenic liquids, including BOG, is critical for the commercial viability of hydrogen ships. Minimizing boiling phenomena requires advanced insulation technologies, underscoring the need for research that takes these factors into account.

Historically, experimental research has concentrated on improving heat transfer efficiency and comprehending the impact of critical heat flux on industrial equipment like boilers, reactors, and cryogenic fluid systems [12]. Bartolomei and Chanturiya [13] elucidated the relationship between flow enthalpy, void-fraction, and temperature in vertical pipes through their experiments, while Robinson [14] detailed the relationship between heat flux, coefficient of heat transfer, and wall temperature in horizontal channels. Even though these experiments did not directly utilize cryogenic fluids, the subcooled boiling phenomena resulting from heating the internal fluid and the effects of bubbles formed on the pipe walls were deemed to have implications for pipe safety.

Recent advancements have seen Computational Fluid Dynamics (CFD) widely applied to analyze thermofluid-related issues, particularly boiling phenomena, dictated by thermal transfer mechanisms [15]. Krepper et al. [16] replicated Bartolomei and Chanturiya's experiments [13] using CFD, comparing simulation results with experimental data. Braz Filho et al. [17] conducted a study on subcooled boiling phenomena based on pressure values, performing a sensitivity analysis on factors affecting the heat transfer coefficient. Gu et al. [18] combined various correlations using a wall boiling model based on Bartolomei and Chanturiya's experiments to describe subcooled boiling phenomena [13]. Furthermore, Langari et al. [19] applied the Rohsenow boiling model in CFD simulations to replicate parts of Robinson's experiments [14], while Ha et al. [20] verified subcooled boiling models under low pressure and Peclet numbers. Chung et al. [12] implemented simulations of Bartolomei and Chanturiya's experiments [13], comparing the sensitivity and convergence between phase-change models and parameters of the wall boiling model. Additionally, Seo et al. [21] analyzed multiphase thermal flow in LH_2 piping of the Cargo Handling System (CHS) for hydrogen transport ships, evaluating the insulation performance based on insulation combinations to assess pipe safety.

Moreover, insulation is as critical as the boiling process for maintaining thermal integrity, with both experimental and CFD simulations having been conducted in this area. Fesmire [22] demonstrated, through experiments, how thermal properties of a vacuum insulation system vary with vacuum pressure using liquid nitrogen. Lim et al. [23] compared insulation performance of vacuum and polyurethane foam (PUF)-based materials in liquid nitrogen piping through simulations. Kim et al. [24] utilized a vacuum insulation system featuring Multi-Layer Insulation (MLI) and vacuum layers for liquid hydrogen piping, performing thermal transfer and structural analyses.

However, recent pipe simulations primarily focus on structural assessments and the measurement of temperature distributions, incorporating insulation. A notable gap exists in the explicit documentation of verification processes for phase-change models, casting doubts on the reliability of these simulations. The paucity of experimental and

CFD analyses specifically addressing liquid hydrogen piping underscores a significant gap in safety evaluation protocols. Additionally, experimental and CFD analysis cases related to liquid hydrogen pipes are scarce. For this reason, the studies by Seo et al. [21] and Kim et al. [24] are significant as they discuss the analysis techniques and results of multiphase thermal flow CFD simulations and thermal–structural CFD simulations for hydrogen pipe, respectively. As previously mentioned, Seo et al. [21] evaluated the performance of insulation systems through multiphase thermal flow analysis and selected insulation materials that minimize heat transfer. Furthermore, they used the LFL of GH_2 as a safety standard for pipe safety evaluation and compared it with the total volume fraction of GH_2 inside the pipe, providing a useful reference for establishing design regulations for LH_2 pipe. Kim et al. [24] identified the design parameters of materials suitable for LH_2 flow based on the mechanical properties, thermal equilibrium, and structural response of pipelines installed in LH_2-fueled ships with cryogenic MVIP and used a sensitivity analysis of these parameters to facilitate computer-aided design engineering research. Consequently, CFD simulation to understand the thermodynamic characteristics of internal fluids due to external heat transfer in liquid hydrogen piping is considered beneficial for the development of regulations related to hydrogen piping infrastructure.

The present study focuses on assessing the insulation performance by examining the thermo-fluid dynamics of hydrogen and identifying an effective insulation system that significantly minimizes heat transfer, achieved through performing a series of multiphase thermal flow simulations that consider the boiling phenomena within insulated liquid hydrogen (LH_2) piping systems for the FGSS of hydrogen-fueled ships. While employing an analytical approach to Seo et al. [21], this study distinguishes itself by focusing on the safety evaluation of LH_2 piping under relatively high-pressure conditions, in contrast to the CHS. The previous research by Seo et al. [19] focused on multiphase thermal flow simulation in the Cargo Handling System (CHS) of an LH_2 carrier, where the system operates at 1.33 bar. In this study, we analyze the piping conditions for the Fuel Gas Supply System (FGSS) in an LH_2-fueled ship under 5 bar conditions, thus termed relatively high-pressure conditions. The safety evaluation tools used include assessments of the volume fraction of GH_2 and comparisons to the Lower Flammability Limit (LFL). Additionally, we evaluate the performance of various insulation materials to determine the optimal configuration for minimizing heat transfer and ensuring safety under these high-pressure conditions. Therefore, it is expected to establish comprehensive guidelines for the design of piping systems for hydrogen-fueled ships and provide useful information to improve safety and operational efficiency.

2. Numerical Methods

In a vacuum-insulated piping, the two-phase flow of liquid and gaseous hydrogen was simulated within the Eulerian–Eulerian framework of a commercial CFD software, STAR-CCM+ (version 16.04.007) (Simens, Munich, Germany). The governing equations for mass, momentum, and energy conservation were defined separately for each phase. The modeling of interactions between various fluid phases was accomplished through the use of interphase force and heat transfer. Specifically, near-wall boiling phenomena, where subcooled liquid is heated due to the temperature difference with the wall and bubbles form at the wall, were accounted for by employing a wall boiling model to ensure accurate modeling of heat transfer near the wall. Additionally, insulation and various materials were assumed to be solid, allowing for the simultaneous analysis of thermal transfer within solids.

2.1. Governing Equations

The Eulerian multiphase model considers each phase as interpenetrating continua and assumes uniform pressure across all phases. Additionally, interactions such as mass, momentum, and energy exchanges between phases are accounted for through respective

interphase force and heat transfer models. First, the continuity equation represents the mass conservation for each phase and is expressed as Equation (1).

$$\frac{\partial}{\partial t}\int_V (\alpha_i \rho_i) dV + \oint_A (\alpha_i \rho_i \mathbf{v}_i) d\mathbf{a} = \int_V \sum_{j \neq i} (\dot{m}_{ij} - \dot{m}_{ji}) dV + \int_V S_i dV \tag{1}$$

where α_i, ρ_i, $\mathbf{v}_i$, and S_i denote the volume fraction, density, velocity vector, and source term of phase i, respectively. The volume fractions must fulfill $\sum \alpha_i = 1$, and $\dot{m}_{ij}$ and $\dot{m}_{ji}$ represent the mass evaporation rate and mass condensation rate, respectively.

Next, the momentum equation describes the temporal change and spatial transport of momentum, representing momentum conservation while accounting for interphase interactions, as shown in Equation (2).

$$\begin{array}{c} \frac{\partial}{\partial t}\int_V (\alpha_i \rho_i \mathbf{v}_i) dV + \oint_A \alpha_i \rho_i \mathbf{v}_i \otimes \mathbf{v}_i d\mathbf{a} = -\int_V \alpha_i \nabla p dV + \int_V \alpha_i \rho_i \mathbf{g} dV + \oint_A \boldsymbol{\tau}_i d\mathbf{a} \\ + \int_V \sum_{i=1}^{n} (\dot{m}_{ji} \mathbf{v}_{ji} - \dot{m}_{ij} \mathbf{v}_{ij}) dV + \int_V \mathbf{S}_i dV + \int_V \mathbf{F}_{ji} dV, \end{array} \tag{2}$$

$$\boldsymbol{\tau}_i = \alpha_i \mu_i \left(\nabla \mathbf{v}_i + \nabla \mathbf{v}_i^T \right) + \alpha_i \left(\lambda_i - \frac{2}{3} \mu_i \right) \nabla \cdot \mathbf{v}_i \mathbf{I} \tag{3}$$

where p is considered uniform across all phases, $\mathbf{g}$ is the gravitational acceleration, $\boldsymbol{\tau}_i$ represents the stress tensor, $\mathbf{v}_{ji}$ and $\mathbf{v}_{ij}$ are velocities between phases, $\mathbf{S}_i$ is the momentum source term, and $\mathbf{F}_{ji}$ includes forces involved in interphase transfer, such as interphase drag, virtual mass force, lift force, turbulent dispersed force, and wall lubrication force. In the momentum equation, the stress tensor for each phase follows the stress tensor model for a viscous fluid, and the gravitational acceleration is applied uniformly.

The energy conservation equation assumes that body forces are applied uniformly, describing the temporal change and spatial transport of energy while accounting for interphase heat transfer, as shown in Equation (4).

$$\begin{array}{c} \frac{\partial}{\partial t}\int_V \alpha_i \rho_i E_i dV + \oint_A \alpha_i \rho_i \mathbf{v}_i H_i \cdot d\mathbf{a} + \oint_A \alpha_i p d\mathbf{a} = \oint_A \alpha_I k_i \nabla T_i d\mathbf{a} + \oint_A \mathbf{T}_i \cdot \mathbf{v}_i d\mathbf{a} + \int_V \mathbf{f}_i \cdot \mathbf{v}_i d\mathbf{a} + \\ \int_V \sum_{j \neq i} Q_{ij} dV + \int_V Q_i^{(ij)} dV + \int_V S_{u,i} dV \end{array} \tag{4}$$

where E_i is the total energy, H_i implies total enthalpy, T_i denotes signifies the temperature of phase i, k_i is the thermal conductivity, $\mathbf{T}_i$ is the viscous stress tensor, $\mathbf{f}_i$ is the body force, Q_{ij} indicates the interphase heat transfer, $Q_i^{(ij)}$ represents the heat transfer from phase i to the interface, and $S_{u,i}$ is the energy source term.

Furthermore, the energy equation for thermal transfer inside solids, including insulation, is provided as Equation (5):

$$\frac{d}{dt}\int_V \rho C_p T dV = -\oint_A \dot{\boldsymbol{q}}'' d\boldsymbol{a} + \int_V S_u dV \tag{5}$$

where ρ is the density of solid, C_p represents the specific heat, T is the solid temperature, $\dot{\boldsymbol{q}}''$ is the heat flux vector, and S_u is defined as the volumetric source term in the solid. According to the principle of energy conservation, the total heat flux is conserved across the fluid–solid interface, necessitating the use of a conjugate heat transfer model at the contact interface [25].

Figure 1 illustrates the exchange of physical quantities at the interface between solids and liquids within a composite heat transfer scenario, as described by Equations (4) and (5). The heat flux traversing the boundary from solid to liquid is represented as $\dot{q}_0$ and $\dot{q}_1$, respectively, and their sum at the solid–liquid interface is conserved following the principle of energy conservation. Temperatures near the boundary for solid and liquid are labeled as T_{c0} and T_{c1}, while temperatures at the interface are indicated as T_{w0} and T_{w1}. Linearized heat flux coefficients, A, B, C, and D, are numerically resolved for each phase.

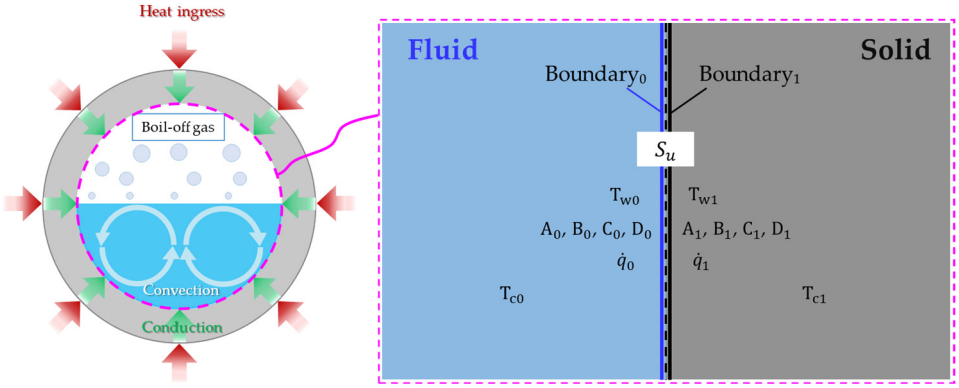

Figure 1. Schematic diagram of conjugated heat transfer between fluid and solid.

2.2. Turbulence Model

Typically, with an increase in Reynolds number, flow transitions from laminar to turbulent, characterized by irregular movements over time. To incorporate turbulence effects in the momentum equation (Equation (2)), Reynolds-averaged Navier–Stokes (RaNS) equations are commonly used. This approach decomposes the flow's velocity components into time-averaged components ($\overline{u}$) and fluctuating components (u'), modeling the resulting Reynolds stress components using the turbulence viscosity coefficient.

To numerically implement such turbulence phenomena, the selection of an appropriate turbulence model is required. In the present study, the Shear Stress Transport (SST) k-ω model, as applied by Seo et al. [19], was chosen for its suitability in analyzing heat transfer associated with phase changes. The SST k-ω model integrates the k-ε and k-ω models, considering the shear stress transmitted in turbulent flows. It combines the benefits of both models, switching to the k-ω model near walls and transitioning to the k-ε model in free-stream regions. In the SST k-ω model, the turbulent viscosity, μ_t, is provided by Equation (6) [26].

$$\mu_t = \rho k T \tag{6}$$

where ρ is the density and T is the turbulent time scale.

The transport equations for turbulent kinetic energy (k) and its specific dissipation rate (ω) are provided by Equations (7) and (8), respectively [26].

$$\begin{aligned} \frac{\partial}{\partial t}\int_V \rho k dV + \oint_A \rho k \overline{v} d\boldsymbol{a} &= \oint_A [(\mu + \sigma_k \mu_t)\nabla k] d\boldsymbol{a} + \int_V P_k dV' \\ &\quad - \int_V \rho \beta^* f_{\beta^*}(\omega k - \omega_0 k_0) dV + \int_V S_k dV \end{aligned} \tag{7}$$

$$\begin{aligned} \frac{\partial}{\partial t}\int_V \rho \omega dV + \oint_A \rho \omega \overline{v} d\boldsymbol{a} &= \oint_A [(\mu + \sigma_\omega \mu_t)\nabla \omega] d\boldsymbol{a} + \int_V P_\omega dV \\ &\quad - \int_V \rho \beta^* f_\beta(\omega^2 - \omega_0^2) dV + \int_V S_\omega dV \end{aligned} \tag{8}$$

where $\overline{v}$ denotes the mean velocity, μ represents the dynamic viscosity, f_{β^*} is the free shear correction factor, f_β is the eddy current stretching correction factor, and ω_0 and k_0 are the atmospheric turbulence values associated with turbulence attenuation. Wilcox [27] defined σ_k and σ_ω as model coefficients set to 0.5 s. The production terms P_k and P_ω account for the generation of turbulent kinetic energy and its dissipation rate, respectively. Turbulent kinetic energy is derived from the contributions of turbulence, buoyancy, and nonlinear production terms, while the specific dissipation rate incorporates terms for dissipation avoidance and cross-diffusion [26].

2.3. Wall Boiling Model

Figure 2 illustrates the process of boiling in a subcooled liquid within an LH_2 pipe. Initially, the liquid is subcooled, meaning its temperature is below the saturation temperature at the given pressure. As the liquid progresses through the pipe, heat is applied to the walls, causing the temperature of the liquid near the wall to increase. This creates a temperature gradient between the liquid near the wall and the bulk liquid, resulting in

convective heat transfer. When the liquid near the wall reaches the saturation temperature, nucleate boiling begins, characterized by the formation of vapor bubbles at discrete sites on the heated wall, known as the Onset of Nucleate Boiling (ONB). These bubbles grow and eventually detach from the wall at the Net Vapor Generation (NVG) point, where the rate of vapor generation exceeds the rate at which the vapor condenses back into the liquid. Beyond the NVG point, the vapor bubbles continue to grow and coalesce as they move away from the wall, leading to an increase in the overall vapor content within the liquid. As the liquid approaches the Saturated Nucleate Boiling (SNB) point, the entire liquid within the pipe reaches the saturation temperature, resulting in a significant increase in vapor generation. At this stage, the flow consists of a mixture of vapor and liquid, with the vapor phase becoming more dominant as the heat flux increases.

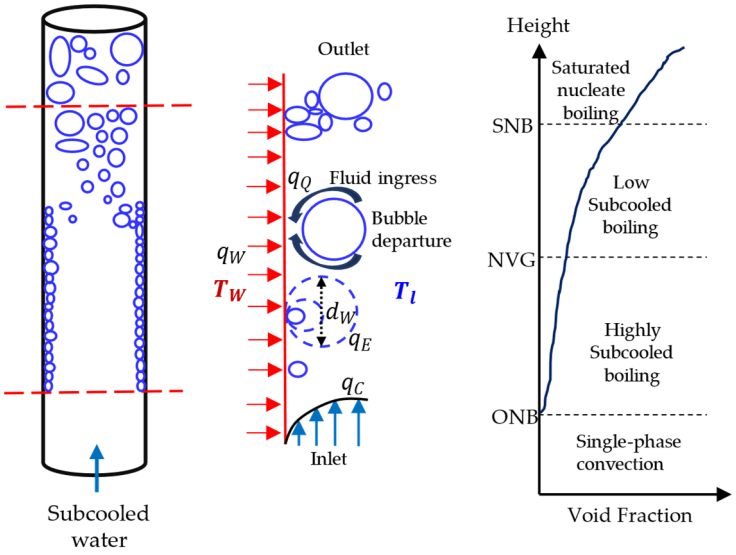

Figure 2. Schematic representation of the wall boiling model. The dashed line in the figure represents SNB and ONB, respectively, from the top.

The wall boiling model, founded on the experimental results of Kurul and Podowski [28], represents a nucleate boiling framework. Figure 2 depicts this model, where the heat flux impinging on the wall is segregated into three distinct components as per Equation (9) upon the entry of subcooled liquid into the pipe. This segregating aids in detailing the bubbles formation process.

$$q_W = q_C + q_Q + q_E \tag{9}$$

Initially, q_C represents the convective heat flux, which denotes the portion of heat flux transferred from the wall that facilitates convection between the incoming liquid at the inlet and the wall, as defined by Equation (10).

$$q_C = h_C(T_W - T_l)(1 - A_b) \tag{10}$$

$$A_b = \min\left(1, K\frac{N_W \pi d_W^2}{4}\right) \tag{11}$$

$$K = 4.8exp\left\{-\frac{Ja_{sub}}{80}\right\} \tag{12}$$

$$Ja_{sub} = \frac{\rho_l C_P \Delta T_{sub}}{\rho_v h_{lat}} \tag{13}$$

where h_C defines the single-phase heat transfer coefficient and T_W and T_l are the wall and liquid temperatures, respectively. A_b is a coefficient dependent on the bubble departure diameter (d_w) and nucleation site density (N_W), K is an empirical coefficient, Ja_{sub} indicates

the subcooled Jacob number, $\Delta T_{sub} = T_{sat} - T_l$ is the subcooling temperature of liquid, and h_{lat} is the latent heat of boiling [1]. The convective heat flux primarily affects the temperature increase in the liquid near the wall, facilitating convection both at the wall and away from it. This creates a temperature boundary layer that affects bubble formation on the wall, which can be defined as the ONB.

Convective heat flux exclusively affects the temperature increase in the liquid adjacent to the wall, initiating convection between the flow close to the wall and the distant flow, thereby forming a thermal layer at which bubbles originate. This phenomenon is known as the ONB.

Furthermore, q_E implies the evaporation heat flux, denoting the portion of the heat flux applied to the wall that contributes to the liquid's boiling, as defined in Equation (14).

$$q_E = V_d N_W f \rho_v h_{lat} \tag{14}$$

$$V_d = \frac{\pi d_W^3}{6} \tag{15}$$

where V_d is the volume of bubbles for each bubble departure diameter and f is the bubble departure frequency as defined by Cole [29].

The evaporation heat flux triggers boiling by vaporizing the liquid near the wall that reached saturation temperature upon crossing the ONB point, leading to bubble formation. Subsequently, q_Q denotes the quenching heat flux, which corresponds to the average heat flux transferred to the liquid filling the space vacated by departing bubbles, as specified in Equation (16).

$$q_Q = \frac{2k_l}{\sqrt{\pi \lambda_l \tau}} A_b (T_W - T_l) \tag{16}$$

where k_l represents the thermal conductivity of the liquid, λ_l denotes the diffusivity of the liquid, and τ is the period of average bubble departure.

The quenching heat flux causes bubbles formed at the wall to detach when they reach the departure diameter at the NVG point. Beyond the SNB point, the entire liquid within the pipe attains saturation temperature. The heat flux component and boiling rate are primarily determined by the nucleation site density (N_W) and bubble departure diameter (d_W). While various correlations derived from experimental studies by researchers are available, the application within STAR-CCM+ is subject to limitations. The models for N_W and d_W provided in STAR-CCM+ are outlined in the subsequent sections.

2.3.1. Nucleation Site Density (N_W)

The nucleation site density, N_W, represents the count of locations per unit area on the heated surface where bubbles emerge, significantly influencing the evaporation rate during boiling events. Lemmert and Chawla [30] presented this concept through an empirical formula, as shown in Equation (18), referred to as the LC model.

$$N_W = C^n (T_W - T_{sat})^n \tag{17}$$

where C and n are coefficients determined empirically from experiments, as investigated Kurul and Podowski [26], with values of 210 and 1.805, respectively. T_W represents the wall temperature, and T_{sat} is the saturation temperature.

Conversely, Kocamustafaogullari and Ishii [31] presented an empirical formula for N_W as depicted in Equation (18), referred to as the KI model.

$$N_W = \frac{f(\rho^*)}{\delta_W} \left(\frac{4\sigma T_{sat}}{\rho_g h_{lat} d_W \Delta T_e} \right)^{-4.4} \tag{18}$$

$$\Delta T_e = \Delta T_{sub} S \tag{19}$$

$$f(\rho^*) = 2.157 \times 10^{-7} (\rho^*)^{-3.2} (1 + 0.00049 \rho^*)^{4.13} \tag{20}$$

$$\rho^* = (\rho_l - \rho_v)/\rho_v \tag{21}$$

where ΔT_e and S are the effective superheated wall temperature and the suppression factor, respectively.

2.3.2. Bubble Departure Diameter (d_W)

The bubble departure diameter, d_W, indicates the diameter of a bubble when it separates from the nucleation site, significantly influencing the evaporation rate in boiling phenomena. Tolubinsky and Kostanchuk [32] introduced an empirical formula for d_W, as demonstrated in Equation (22), with a stipulated minimum bubble departure diameter of 1.4 mm, known as the TK model.

$$d_W = \min\left(0.0014, 0.006exp\left\{-\frac{\Delta T_{sub}}{45.0}\right\}\right) \tag{22}$$

Meanwhile, Kocamustafaogullari and Ishii [31] presented an empirical formula for d_W, referred to as the KI model.

$$d_W = 0.0012(\rho^*)^{0.9}\left[\frac{\sigma}{g(\rho_l - \rho_v)}\right] \tag{23}$$

where ϕ represents the contact angle formed between the wall and bubble. Rogers and Li [33] determined ϕ to be 80°.

2.4. Validation of Wall Boiling Model

To ensure the accuracy of the wall boiling model, a validation simulation was conducted prior to simulating multiphase thermal flow in LH_2 piping. Selected cases from experiments by Robinson [14], illustrated in Figure 3, served as the basis. In these experiments, a 10 × 10 × 50 (mm) heating block was placed 76 mm below a 16 × 10 × 241 (mm) horizontal channel. A mixture of water and antifreeze in a 50:50 ratio was introduced, allowing for variations in pressure and heat flux, and thus enabling the measurement of wall temperatures. Although Robinson's experiments utilized antifreeze, making the conditions different from those in simulations of liquid hydrogen piping in this study, implementing these phenomena in numerical simulations from the perspective of phase-change mechanisms alone is expected to enhance the reliability of subsequent simulation results.

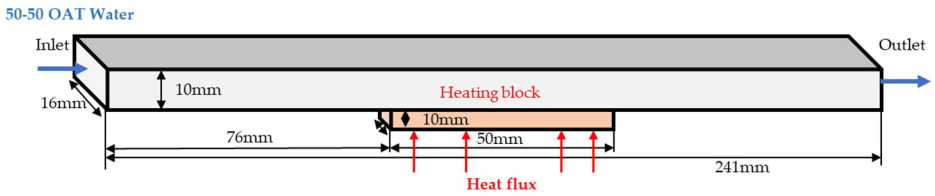

Figure 3. Description of boiling channel.

The conditions and setup for the multiphase thermal flow simulation were set as shown in Figure 4, with a two-dimensional simulation chosen to minimize computational time. Additionally, the anticipated velocity profile within the channel was illustrated. While the experiments involved wall temperature by applying heat flux to a heating block, this simulation streamlined the approach by directly applying heat flux to the wall, thereby defining the area subjected to heating as the 'Heating Wall'. Considering the entrance length (L) calculated as 123 mm, based on $L \approx 10D_h$, the flow transitions from the entrance region to the fully developed region by the end edge of the 'Heating wall' area. The simulation applied velocity inlet conditions at the entrance and outlet conditions at the exit. Boundary conditions and mixture properties are presented in Table 1. The initial pressure for the simulation was set at 2 bar, with five heat flux scenarios identified and compared for their impact on wall temperatures, as outlined in Table 1.

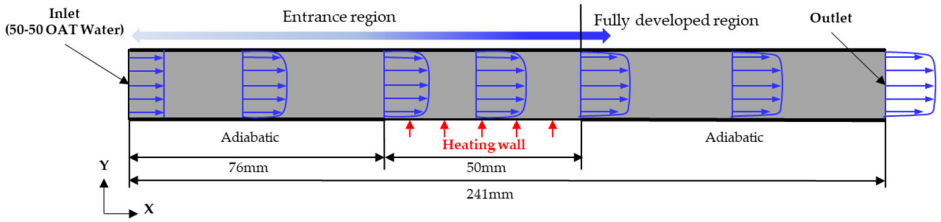

Figure 4. Simulation setup for wall boiling channel.

Table 1. Boundary conditions and liquid properties of validation.

Boundary Condition		Liquid Property	
Inlet temperature	90 °C	Density	1038 kg/m^3
Inlet velocity	0.25 m/s	Dynamic viscosity	0.00085 Pa·s
Inlet	Velocity inlet	Thermal conductivity	0.424 W/mK
Outlet	Outlet	Specific heat	3620 J/kgK
Heat flux	230, 410, 760, 1068, 1350 kW/m^2	Boiling temperature	108 °C
		Pressure	2 bar

Figure 5 depicts the temperature field, vaporization rate, and velocity field for the most severe case among the five heat flux scenarios, specifically at 1350 kW/m^2. It shows how thermal energy is transmitted to the internal fluid, leading to a temperature increase due to the heat flux supplied from the wall within the heating wall area. This process results in the formation of numerous bubbles adjacent to the wall. In the velocity field, one can observe a gradual increase in speed starting from the points where bubbles are formed, culminating in a sharp acceleration of velocity from the end of the heating wall onwards. This phenomenon seems to be attributed to the rising of the bubble clusters formed on the wall due to buoyancy.

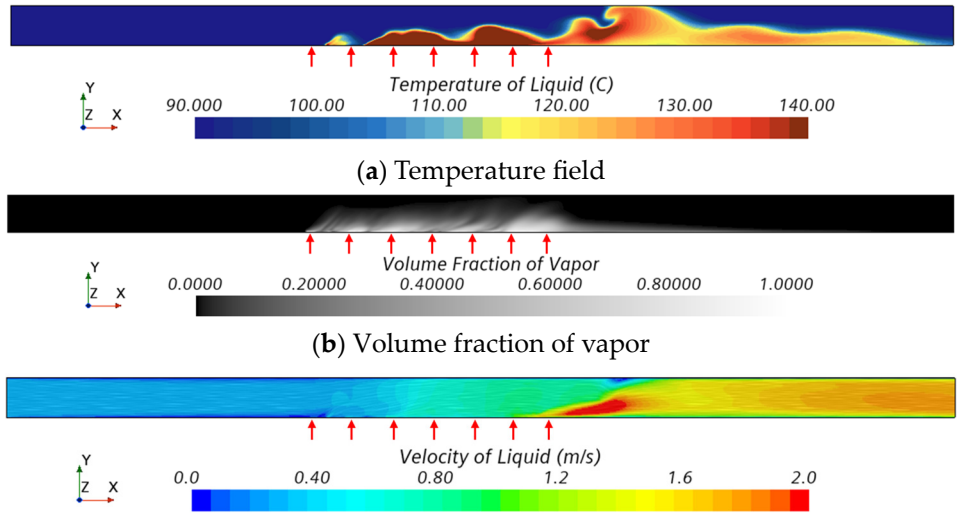

(**a**) Temperature field

(**b**) Volume fraction of vapor

(**c**) Velocity field

Figure 5. Simulation results (heat flux: 1350 kW/m^2). The arrow explains heat flux region.

Figure 6 displays the comparison between temperatures of the heating wall as simulated in five heat flux scenarios and their corresponding experimental data. Employing the wall boiling model, the simulation results closely match the experimental data, with an error margin ranging between 0.3 and 1.4%. Consequently, the validation simulation of the wall boiling model confirms the accuracy of the phase-change model, enabling its application in the subsequent simulations of multiphase thermal flow in LH_2 piping.

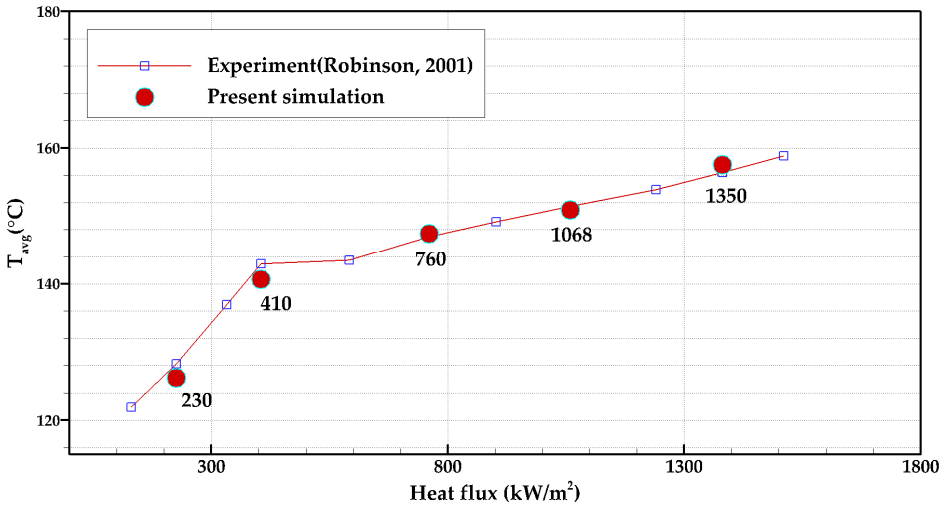

Figure 6. Comparison of experiment [14] and simulation results by different heat flux.

3. Numerical Simulation

In this study, the FGSS for a hydrogen-propelled ship, targeted for analysis, comprises two lines within the liquid hydrogen piping, as illustrated in Figure 7. One line transports liquid hydrogen from the fuel tank to the Pressure Build Up (PBU) unit, referred to as the PBU inlet line. The other transports liquid hydrogen to the vaporizer, known as the LH_2 fuel line. These two lines are the focus for the multiphase thermal flow simulation within the FGSS piping, assuming only liquid hydrogen is introduced. The piping design references the ASME and IGC codes, known for their cryogenic fluid piping design standards. While the overall process of this study mirrors the research conducted by Seo et al. [21], the differing pressures and temperatures of LH_2 necessitate the re-selection of pipe diameter and thickness. Additionally, it aims to evaluate the safety of the piping under conditions of relatively higher pressure compared to those typically encountered in Cargo Handling System (CHS).

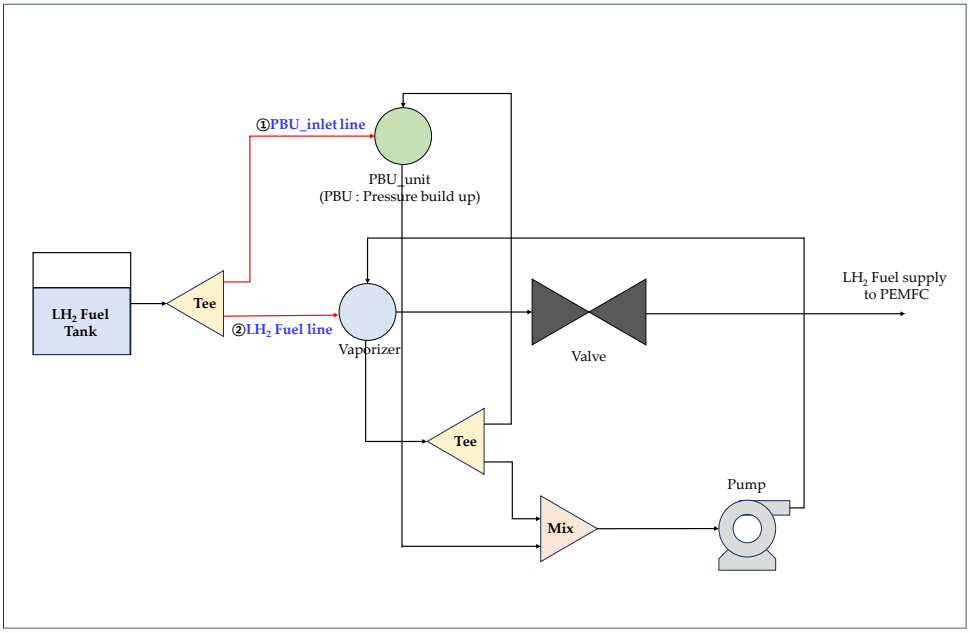

Figure 7. Schematic diagram of FGSS lines.

The cross-sectional configuration and selected materials for the FGSS piping are presented in Figure 8. The internal passage is designated for LH_2 flow, utilizing SUS316L

for the inner piping due to its excellent corrosion and rust resistance, making it ideal for cryogenic fluid transport. The outer shell employs carbon steel to withstand external pressure and form a vacuum space. Insulation considers a high-performance vacuum insulation system as the base for transporting LH_2 at approximately −253 °C, with variations in the internal filler material. Various filler materials were applied under a vacuum pressure of 5×10^{-5} Torr (5 millitorr), including solely vacuum conditions, and the thermal properties at that vacuum pressure were used. The selected composite vacuum insulation system consists of combinations like vacuum + (aerogel blanket, aerogel particle, fiberglass, glass bubble, Multi-Layer Insulation (MLI) Mylar net, and perlite powder), with PUF (polyurethane foam) also chosen for comparison due to its frequent use in LNG storage and transport insulation. The physical properties of these insulation materials were referenced from Fesmire [22] and are detailed along with other materials in Table 2.

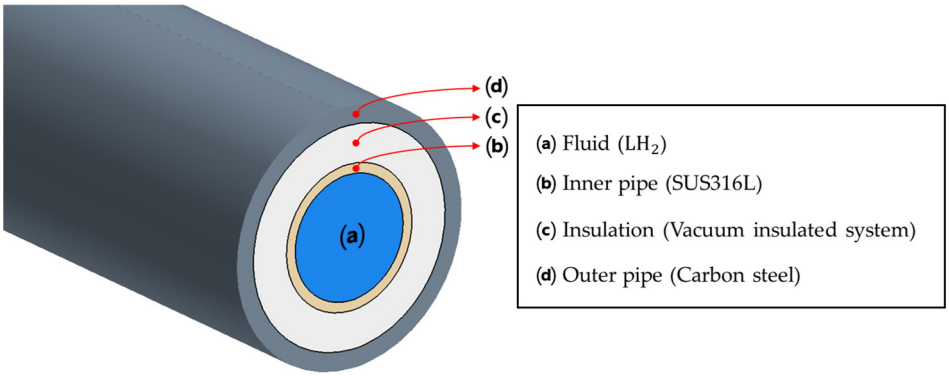

Figure 8. FGSS pipe composition.

Table 2. Material properties of pipe composition [22].

Type	Density (kg/m^3)	Specific Heat (J/kgK)	Thermal Conductivity (W/mK)
SUS316L	7750	502	15.1
Carbon steel	7850	464.7	60.5
Only vacuum	1.225	1005	0.010746
Vacuum + aerogel blanket	133	943	0.001461
Vacuum + aerogel particle	80	700	0.00171
Vacuum + fiberglass	16	700	0.001912
Vacuum + glass bubble	65	750	0.000695
Vacuum + MLI Mylar net	42	1300	0.000254
Vacuum + perlite powder	132	837	0.000947
PUF	16	1200	0.024

The inner diameter of the piping was determined by considering the flow rate among the initial conditions for LH_2, referencing the fluid velocity limit of 12 m/s as outlined in the International Association of Classification Societies (IACS) in their LNG bunkering rule [34]. The fluid velocity of 3 m/s applied to the practical pipe design is employed in the present study. Using the Diameter Nominal (DN) notation in millimeters as shown in Table 3, analysis cases for each line were selected. It was expected that variation in pipe diameter would influence fluid velocity, potentially leading to differences in internal flow characteristics and heat transfer phenomena. Therefore, to determine the appropriate diameter, two diameter cases per line were considered.

Table 3. Diameter of LH_2 pipe in FGSS [34].

Case No.	Property	Mass Flow (Ton/Day)	Diameter (mm)	DN (Dimensionless)	Velocity (m/s)
1	PBU inlet line	0.5	13.72	8	1.14
2			17.14	10	0.65
3	LH_2 fuel line	3.54	26.67	20	1.7
4			33.4	25	1.11

The thicknesses of both the inner and outer shells were determined using the pipe thickness formula outlined by the Korean Register (KR), detailed in Equation (24) [35].

$$t = \frac{t_0 + b + c}{1 - \frac{a}{100}}, \tag{24}$$

$$t_0 = \frac{PD}{2Ke + P}, \tag{25}$$

$$b = \frac{Dt_0}{2.5r}, \tag{26}$$

where t_0 is the theoretically required thickness calculated dependent on design pressure, a represents the negative manufacturing tolerance for pipe thickness, b is the allowance thickness for bending processing, c is the allowance thickness for corrosion, P is the design pressure, D represents the outer diameter, K is the allowance stress, e represents the joint efficiency, and r is the inner diameter of the pipe.

Table 4 lists the thicknesses of the inner and outer pipe, calculated per Equation (24) for each case, ensuring compliance with the minimum thickness standards prescribed by DNV-GL [36]. The values in Table 4 were calculated using a design pressure of 5 bar.

Table 4. Thickness of inner/outer pipe in FGSS (unit: mm) [35,36].

Case No.	Property	t (for Inner)	t (for Outer)
1	PBU inlet line	1.65	3.0
2		1.65	3.2
3	LH_2 fuel line	2.1	3.9
4		2.8	4.5

4. Results and Discussions

4.1. LH_2 Flow Characteristics in Pipe

The thermal properties of liquid hydrogen utilized in the simulations, including considerations for the boiling point's dependency on pressure, are detailed in Table 5. The boiling point of LH_2 was determined based on pressure data obtained from National Institute of Standards and Technology [37], as illustrated in Figure 9. In this study, it was assumed that only fully developed LH_2 enters at the inlet, and due to the flow of LH_2 along the pipe, a pressure drop occurs at the outlet, leading to a decrease in the boiling point. To reflect this phenomenon, pressure-dependent boiling points as depicted in Figure 9 were applied.

For the simulation, liquid hydrogen was modeled under the assumption of a fully developed flow regime, adopting a velocity profile based on the modified power law as formulated by Salama et al. [38], detailed in Equation (27).

$$\frac{u}{u_{max}} = \left[1 - \left(\frac{r}{R}\right)^m\right]^{\frac{1}{n}} \tag{27}$$

where r and R represent the radial position and the radius of the pipe and m and n are the exponent coefficients determining the velocity profile, respectively.

Table 5. LH_2 properties in FGSS [37].

	Value
Density (kg/m^3)	60.73
Temperature (°C)	−246.03
Specific heat (J/kgK)	16,416
Thermal conductivity (W/mK)	0.0999
Viscosity (Pa·s)	8×10^{-6}
Surface tension (N/m)	0.000761
Pressure (bar)	5.00

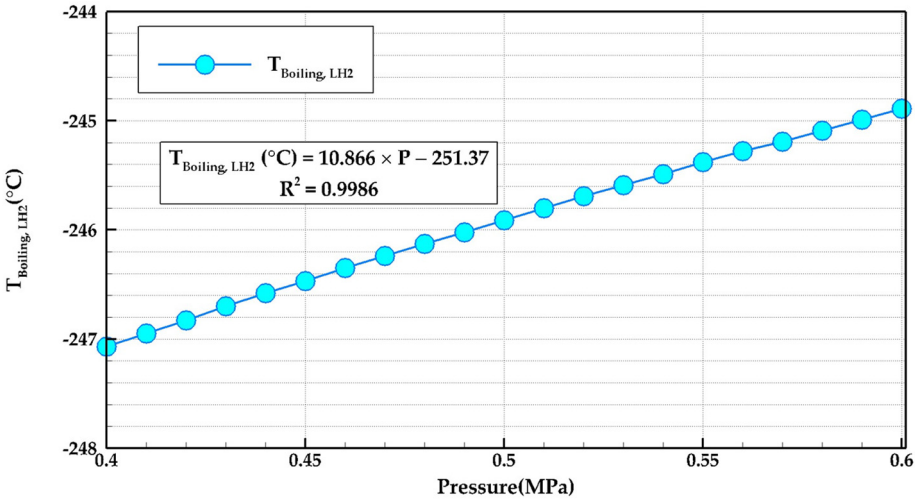

Figure 9. Boiling points by pressure change in FGSS condition [37].

Figures 10–17 depict the results from multiphase thermal flow simulations tailored to various combinations of composite insulation systems and pipe diameter sizes, aligned with Cases 1–4. These illustrations reveal the internal temperature profiles adjacent to the outlet area of the LH_2 piping, alongside the radial temperature gradients observed at the outlet cross-section, for eight unique insulation material combinations. These figures allow for a comparative analysis of the performance of each insulation material.

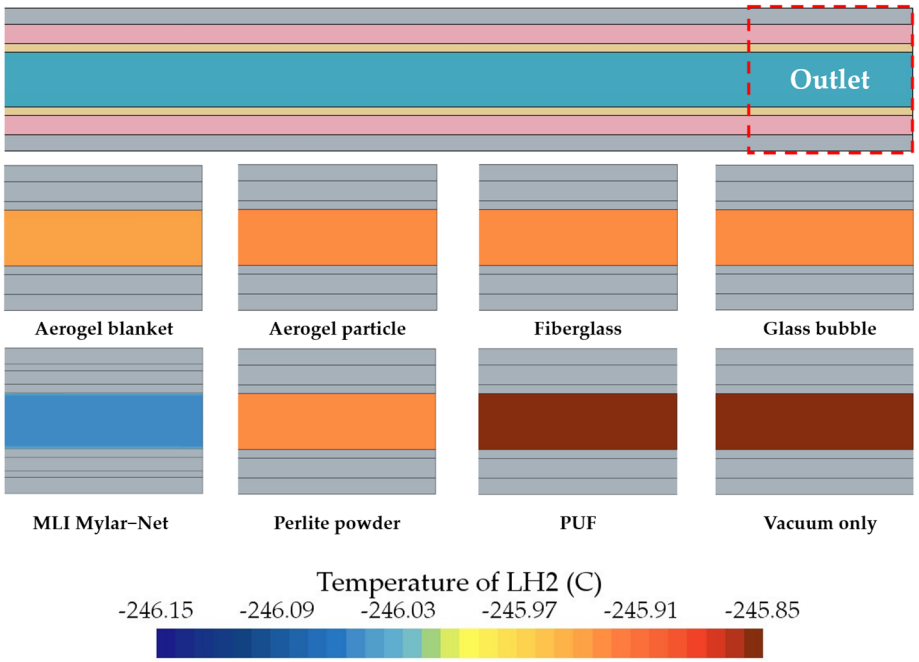

Figure 10. Temperature fields near outlet for various insulations (Case 1).

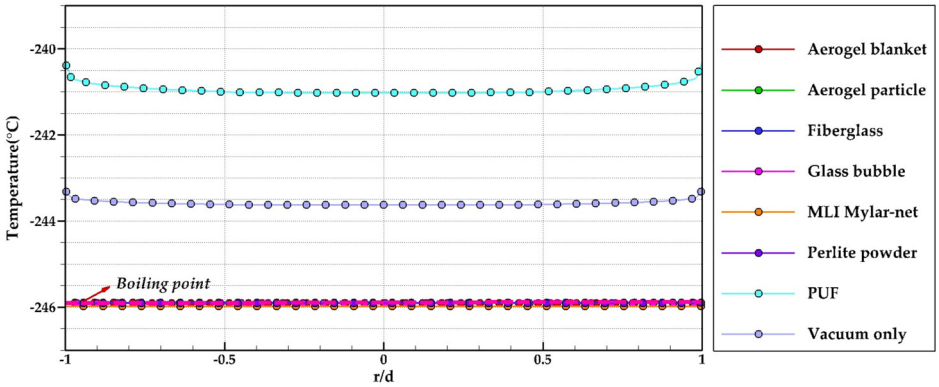

Figure 11. Radial distribution of temperature along vertical centerline at outlet (Case 1).

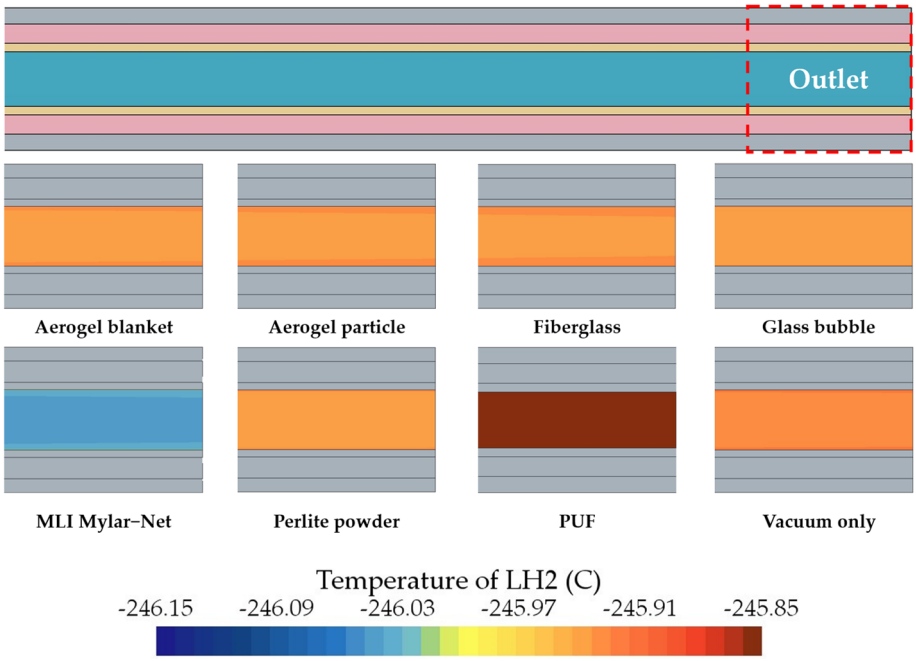

Figure 12. Temperature fields near outlet for various insulations (Case 2).

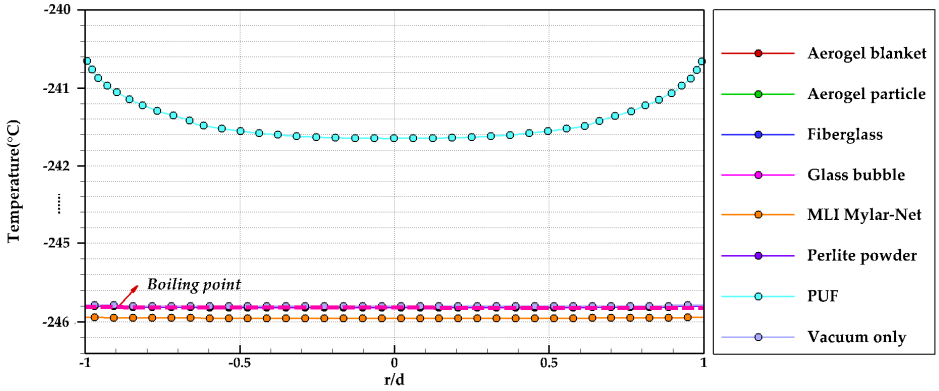

Figure 13. Radial distribution of temperature along vertical centerline at outlet (Case 2).

First, examining the results for Cases 1 and 2, corresponding to the PBU inlet line transporting liquid hydrogen from the fuel tank to the PBU, as shown in Figures 10–13, it is evident that the type of insulation significantly affects the temperature distribution. Specifically, insulation materials with higher thermal conductivities result in higher temperatures. When using PUF or vacuum-only as the insulation material, it is inferred that

the liquid hydrogen reaches temperatures above its boiling point (−246.03 °C), leading to vaporization. Conversely, aerogel blanket, aerogel particle, fiberglass, glass bubble, and perlite powder materials exhibit similar temperature distributions near the boiling point. On the other hand, the use of MLI Mylar net results in negligible temperature variations.

For both Cases 1 and 2, the temperature fields and radial temperature distribution show that using PUF or vacuum-only insulation leads to higher temperatures, indicating a higher risk of LH_2 vaporization, while MLI Mylar net consistently demonstrates superior insulation performance with minimal temperature changes. In Case 2, which involves a larger pipe diameter, the increased heat transfer area results in more heat being transferred, making the differences in insulation performance more pronounced. MLI Mylar net maintains the lowest temperature rise, whereas PUF shows a significant increase in temperature, posing a higher risk of vaporization compared to Case 1.

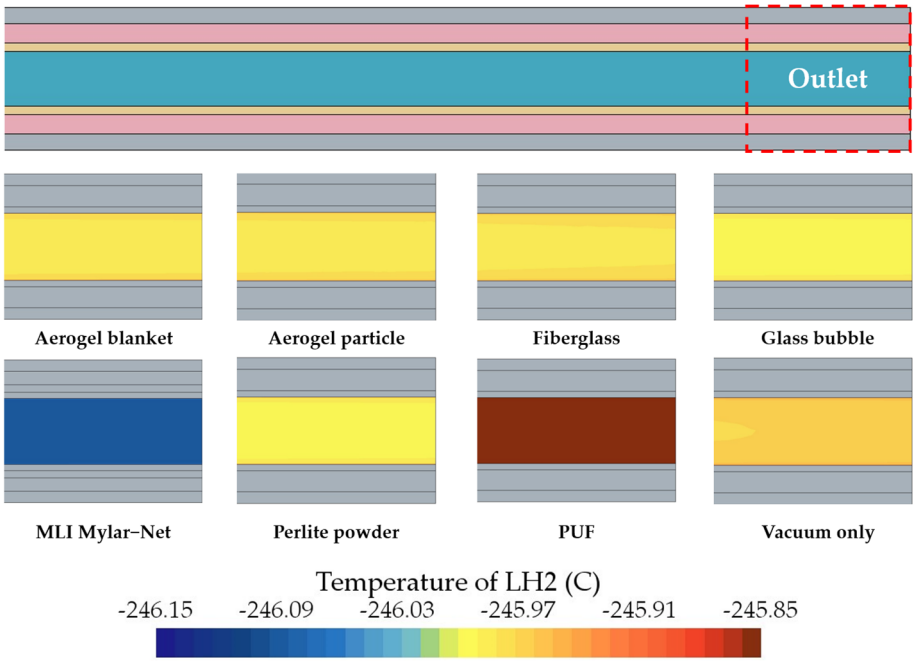

Figure 14. Temperature fields near the outlet for various insulations (Case 3).

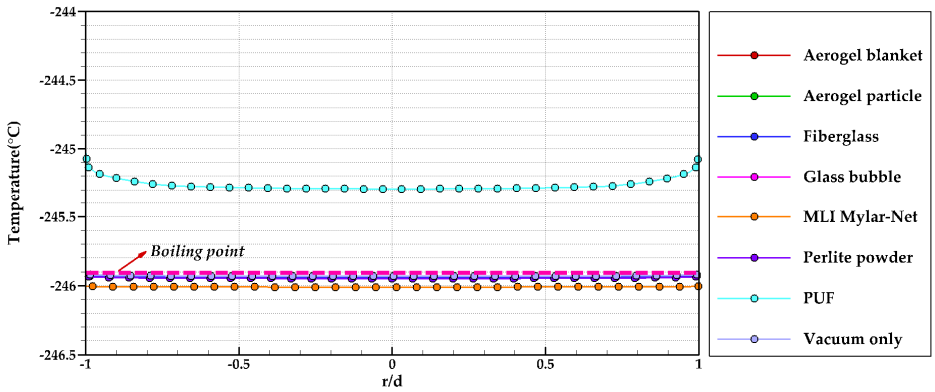

Figure 15. Radial distribution of temperature along vertical centerline at outlet (Case 3).

Next, the results for Cases 3 and 4, associated with the LH_2 fuel line that transports LH_2 from the fuel tank to the vaporizer, can be observed in Figures 14–17. These results indicate that PUF insulation, which leads to temperatures exceeding the boiling point, is unsuitable for LH_2 piping. Conversely, most other insulation materials demonstrate temperatures close to the boiling point, confirming their appropriateness. However, except for the cases using MLI Mylar net, it appears challenging to ensure the intact transfer of

liquid hydrogen in all cases, as the internal temperature of the liquid hydrogen within the piping reaches the boiling point, leading to vaporization into gaseous hydrogen.

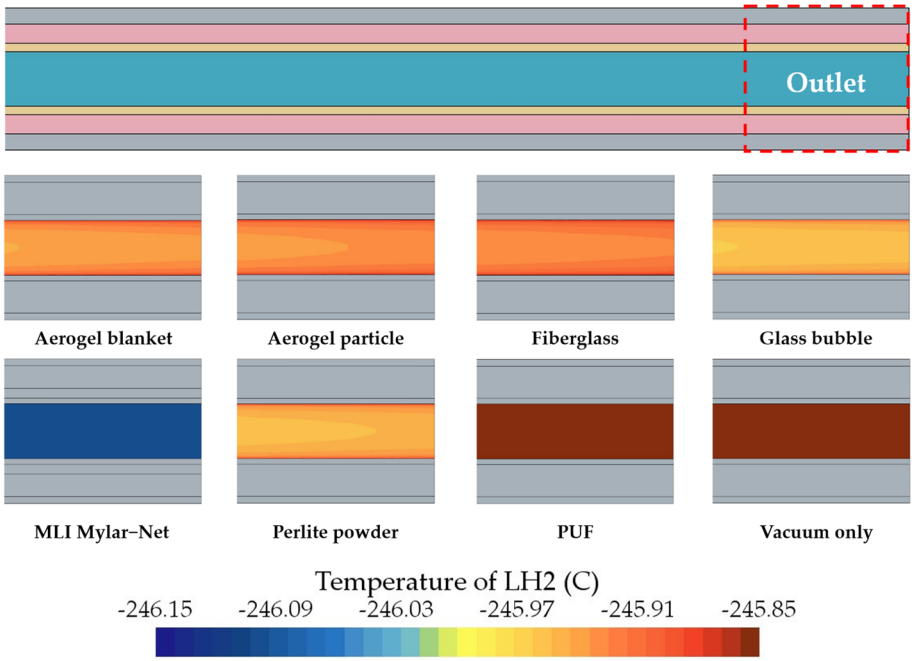

Figure 16. Temperature fields near outlet for various insulations (Case 4).

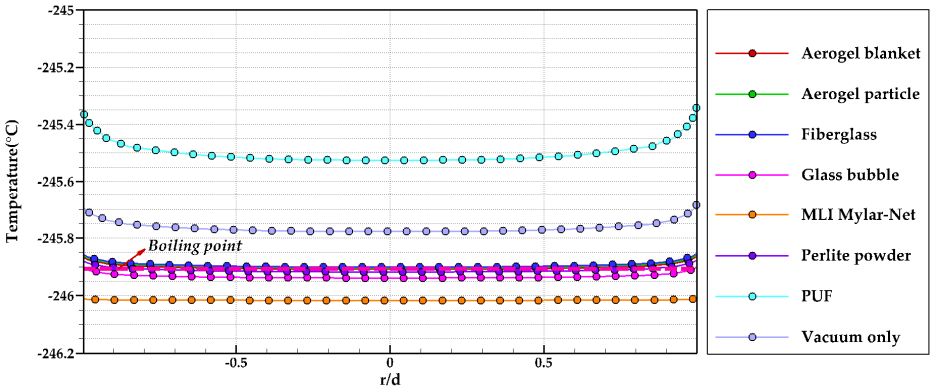

Figure 17. Radial distribution of temperature along vertical centerline at outlet (Case 4).

Furthermore, the temperature of the liquid hydrogen in the FGSS piping was higher in Cases 1 and 2, which were modeled with smaller diameters. This suggests that careful consideration should be given to selecting the diameter size. Similarly, in Cases 3 and 4, which pertain to the LH_2 fuel line, the temperature fields and radial temperature distribution indicate that PUF insulation leads to significant temperature rises, increasing the risk of vaporization, while MLI Mylar net maintains relatively low temperatures. Case 4, with an even larger pipe diameter than Case 3, further emphasizes the superior performance of MLI Mylar net in minimizing temperature changes and preventing LH_2 vaporization. The larger diameter in Case 4 amplifies the impact of insulation materials, with MLI Mylar net consistently outperforming other insulation options.

Figures 10–17 demonstrate that the performance of insulation materials significantly affects the temperature distribution and heat transfer characteristics in LH_2 piping. MLI Mylar net consistently shows superior insulation performance by maintaining the lowest temperature rise, while PUF and vacuum-only insulation leads to higher temperatures and a greater risk of vaporization. The comparative analysis of Cases 1 and 2 versus Cases 3 and 4 highlights that larger pipe diameters increase the heat transfer area, mak-

ing the effectiveness of the insulation material even more critical for safe and efficient LH_2 transportation.

In fully developed laminar and turbulent pipe flows, wall shear stress, τ_W, becomes zero at the center and maximizes at the pipe wall. The relationship is described through the pressure gradient, as detailed in Equation (28) [39–41].

$$\tau_W = -\frac{r}{2}\frac{\partial P}{\partial x} \tag{28}$$

where r represents the inner pipe diameter and $\partial P/\partial x$ denotes the pressure gradient in the flow direction.

Figures 18–21 depict the pressure gradient along the centerline, wall shear stress as determined by Equation (28), and the volume fraction of GH_2 at the wall for the vacuum-only scenarios in Cases 1 to 4. These figures emphasize the effect of bubble generation on the internal flow dynamics, highlighting the significance of accurately identifying the ONB point—where bubbles begin forming in subcooled flow, as indicated by the black dotted lines. Identifying the ONB point, which marks the transition from single-phase to two-phase flow and significantly affects heat transfer and pressure drop in the piping, is crucial for evaluating thermal efficiency and safety [42].

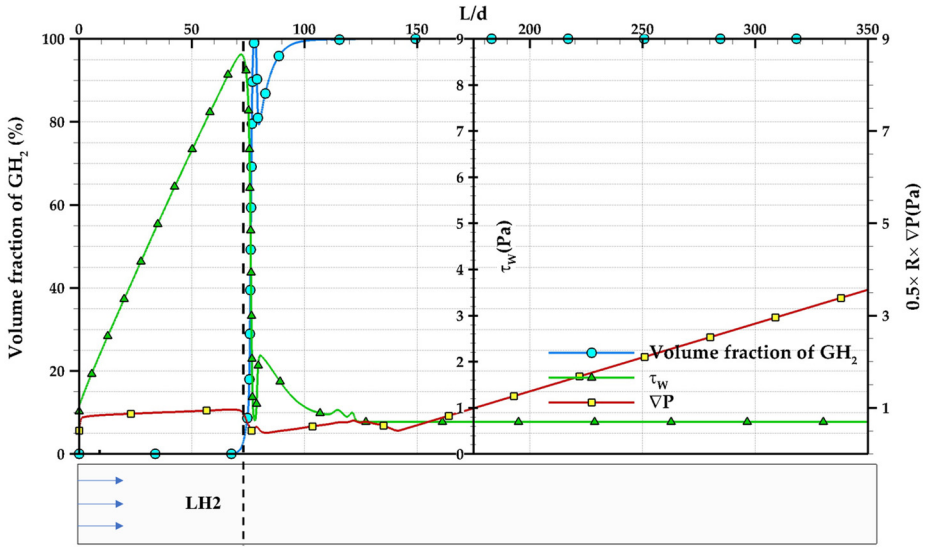

Figure 18. The correlation among ∇P, τ, and volume fraction of GH_2 along the pipeline (Case 1: vacuum only).

In Figure 18, for Case 1, bubble initiation is observed approximately 1 m from the inlet, leading to a reduction in wall shear stress and the emergence of a backpressure gradient as wall vaporization attains 100%. This effect, indicative of bubbles obstructing flow and causing separation, is likely to degrade transport efficiency and, with prolonged piping, compromise safety, suggesting that relatively smaller diameters are ill-suited for LH_2 piping. In contrast, for Cases 2 to 4, as demonstrated in Figures 19–21, the ONB points are detected at comparatively earlier distances of 0.41 m, 0.48 m, and 0.45 m, respectively, where both shear stress and pressure gradient attain their lowest values at the ONB, aligning with Seo et al. [21]'s observations. This early bubble formation and subsequent increase in vaporization underscore the role of precocious ONB identification in boosting heat transfer and elevating vaporization rates.

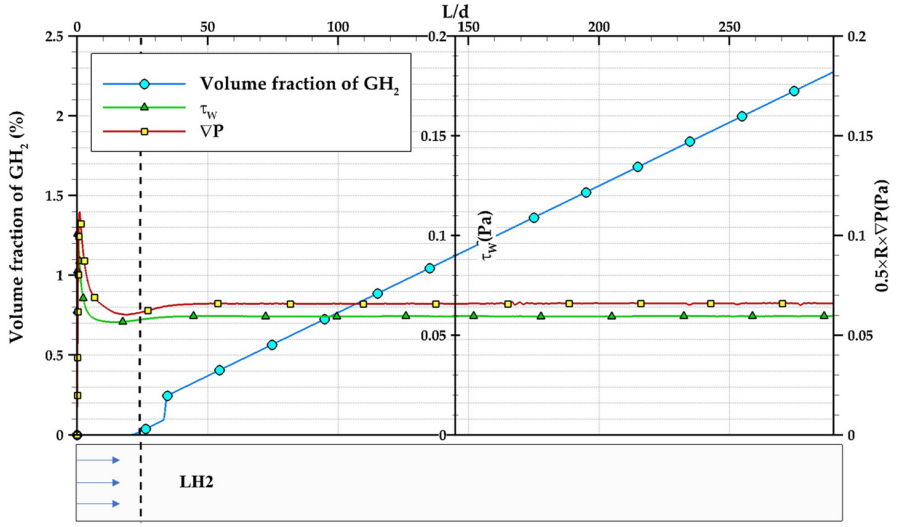

Figure 19. The correlation among ∇P, τ, and volume fraction of GH_2 along the pipeline (Case 2: vacuum only).

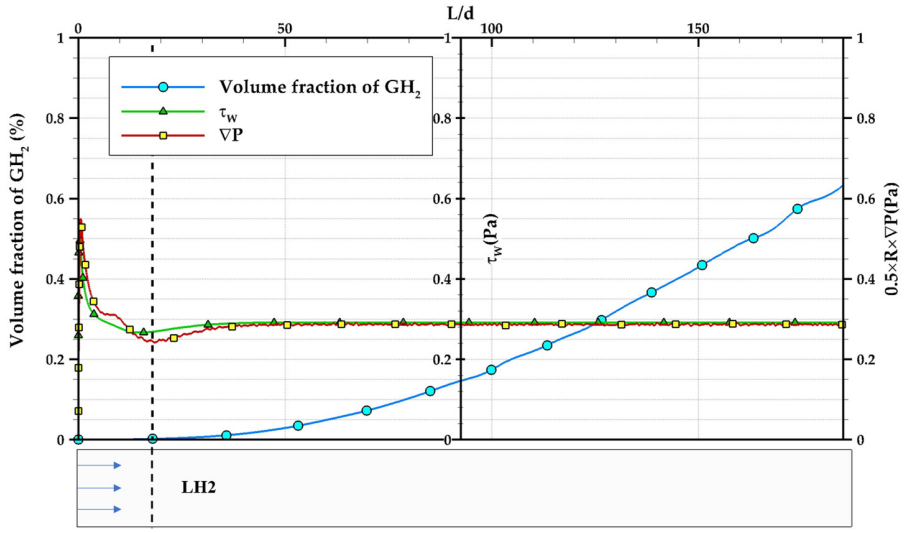

Figure 20. The correlation among ∇P, τ, and volume fraction of GH_2 along the pipeline (Case 3: vacuum only).

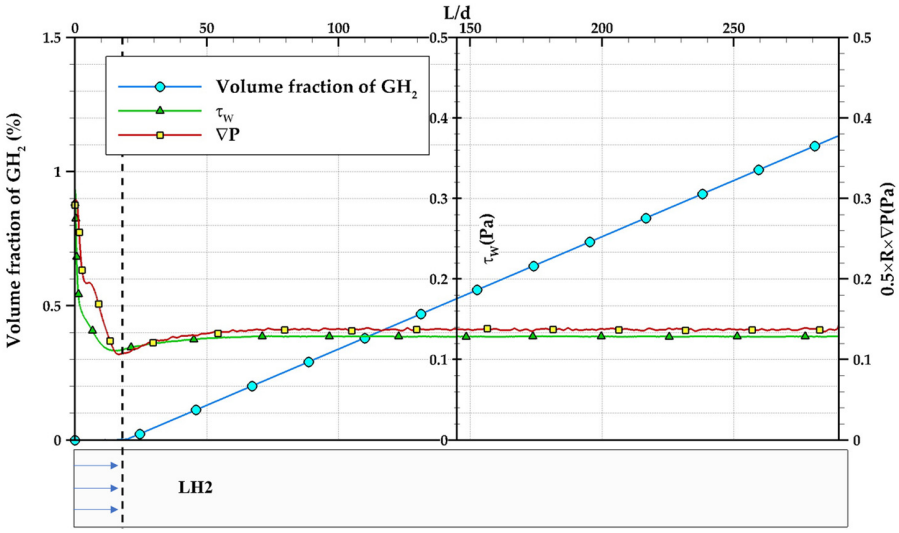

Figure 21. The correlation among ∇P, τ, and volume fraction of GH_2 along the pipeline (Case 4: vacuum only).

Bubble formation and heat transfer become more complex in turbulent flow. Turbulence induces more vigorous mixing compared to laminar flow, which can increase the heat transfer coefficient and accelerate the vaporization rate of liquid hydrogen. However, bubble formation in turbulent flow is irregular, potentially causing localized overheating and pressure fluctuations. This complexity is depicted in Figures 18–21, where the volume fraction of GH_2 increases along the pipe length (L/d), indicating enhanced vaporization due to turbulent mixing. The wall shear stress varies along the pipe length, reflecting the irregular nature of bubble formation and its impact on flow dynamics. The pressure gradient also changes along the pipe length, illustrating the rapid pressure fluctuations associated with turbulent flow. Therefore, accurately identifying and managing the ONB point in turbulent flow, as indicated by the changes in these metrics, is essential to maintaining thermal efficiency and system safety.

4.2. Evaluation of Insulation Performance of FGSS Piping

Insulation is a critical component in pipelines transporting cryogenic fluids, minimizing heat ingress, which is especially vital when transporting cryogenic fluids like hydrogen. Selecting suitable insulation to carry hydrogen in its liquid state is imperative to minimize BOG caused by external heat ingress, thereby enhancing transport efficiency. The present study assesses the thermal performance through the calculation of the heat transfer across the inner wall of composite vacuum insulation. Furthermore, it compares the vaporization rate of LH_2 according to different filler combinations within the vacuum insulation.

Figures 22 and 23 showcase the comparison of heat transferred from the insulation to the inner wall for Cases 1 to 4, reflecting various insulation combinations. As indicated by the thermal conductivity values, the insulation performance ranks from best to least effective as follows: MLI Mylar net > glass bubble > perlite powder > fiberglass > aerogel particle > aerogel blanket > only vacuum. Additionally, in Cases 3 and 4, which feature larger diameters, an increase in the heat transfer area results in a higher amount of heat being transferred compared to Cases 1 and 2.

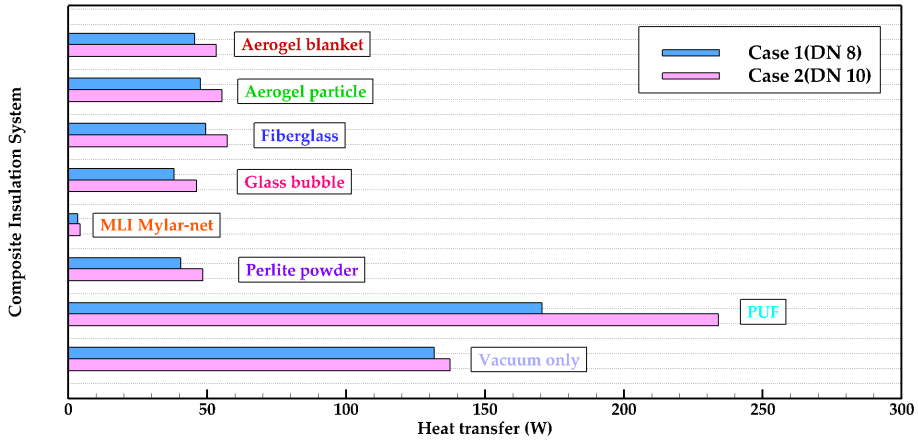

Figure 22. Comparative analysis of heat transfer in PBU inlet line (Cases 1 and 2).

Additionally, the vaporization rates within the pipe, influenced by insulation combinations, are detailed in Table 6 based on the results depicted in Figures 18–21 for each case. In Case 1, regardless of the insulation type, 100% vaporization of LH_2 occurs within the pipe. Such a figure exceeds the LFL of 4%, characteristic of hydrogen gas, which poses a risk of combustion in enclosed spaces. Therefore, pipes with smaller diameters, as in Case 1, are deemed unsuitable for LH_2 piping due to the significant risk of reaching concentrations above the LFL. Conversely, Cases 2 to 4 demonstrate vaporization rates below the LFL, indicating relatively safer conditions.

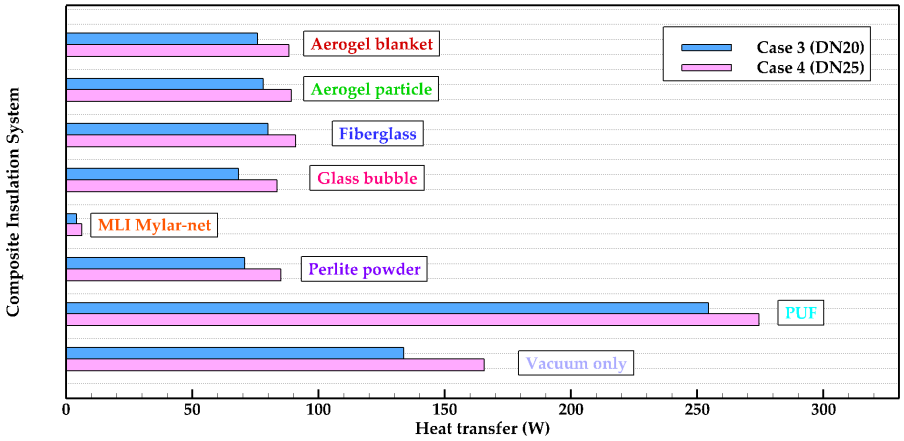

Figure 23. Comparative analysis of heat transfer in LH_2 fuel line (Cases 3 and 4).

Table 6. Total volume fraction of GH_2 in a FGSS pipe (unit: %).

	Case 1	Case 2	Case 3	Case 4
Vacuum only	100	2.3	0.5	0.6
Vacuum + aerogel blanket	100	2.13	0.03	0.17
Vacuum + aerogel particle	100	2.2	0.04	0.2
Vacuum + fiberglass	100	2.18	0.05	0.2
Vacuum + glass bubble	100	1.5	0.006	0.04
Vacuum + MLI Mylar net	100	0.5	0	0
Vacuum + perlite powder	100	1.7	0.01	0.05

Next, Figure 24 illustrates the vaporization rates within the piping as a function of pipe length for Cases 2, 3, and 4, focusing on the vacuum-only case where the highest rates of vaporization were observed. It allows for the estimation of pipe lengths at which the vaporization rate reaches the 4% lower flammability limit (LFL) for hydrogen gas. For Case 2, the vaporization exceeds the LFL at the pipe length of approximately L/d = 700; for Case 3, around L/d = 506; and for Case 4, near L/d = 479, indicating the necessity for a safety review.

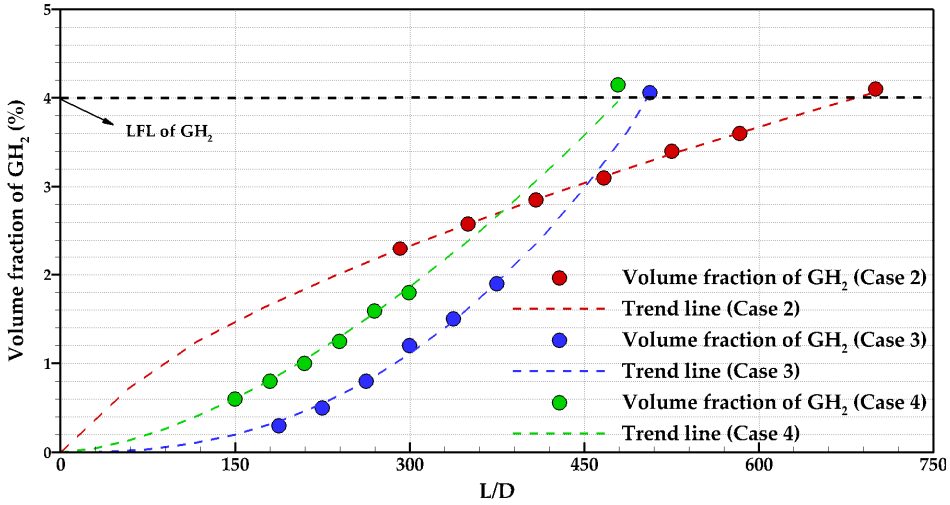

Figure 24. Volume fraction of GH_2 as a function of pipe length.

However, it is important to note that these results were derived from a simplified configuration that did not account for pipe connections or welding, suggesting potential discrepancies with real-world scenarios. Future studies should incorporate these factors for a more accurate assessment.

5. Conclusions

In this study, a series of numerical investigations focused on the multiphase thermal flow dynamics within the vacuum-insulated LH_2 pipelines used in the FGSS of hydrogen-fueled vessels were carried out, specifically concentrating on the phase-change phenomena of the internal fluid. The study yields several key insights:

(1) The selection of piping dimensions and insulation configurations was informed by existing design regulations for cryogenic fluid transportation as outlined in the ASME Code, IGC Code, and various classification society guidelines. We applied a composite vacuum insulation system, combining vacuum insulation with six different fillers, as the primary insulation method in this study. Additionally, we compared and validated the insulation performance using polyurethane foam (PUF), a commonly used LNG insulation material, to assess its effectiveness and feasibility.

(2) Multiphase thermal flow simulations under realistic operational conditions factored in the variable boiling points due to pressure changes, elucidating critical aspects such as bubble nucleation sites on the pipe walls and elucidating the relationship between pressure gradients and shear stresses across different piping scenarios.

(3) Comprehensive multi-physics simulations were undertaken for two distinct piping configurations within each FGSS line, integrating both thermal insulation conductivity and the internal liquid hydrogen's phase-change considerations. This facilitated a quantitative evaluation of insulation performance across various systems, ranking them in descending order of effectiveness as follows: MLI Mylar net > glass bubble > perlite powder > aerogel blanket > fiberglass > aerogel particle > vacuum-only.

(4) The present study also quantified the vaporization rates within the piping, assessing these against the lower flammability limit (LFL) of 4% for hydrogen gas. Notably, smaller diameter pipes, as exemplified in Case 1, demonstrated 100% vaporization irrespective of insulation type, underscoring the critical need for careful selection of pipe diameters in hydrogen FGSS applications.

This investigation's methodological approach to simulating straight-pipe multiphase thermal flows provides valuable insights into fluid behavior within liquid hydrogen FGSS pipelines, offering a foundational basis for developing safety standards and regulatory guidelines. Anticipated future work will extend these analyses to curved pipeline configurations within hydrogen FGSS, addressing the need for detailed flow characteristic studies and associated stress analyses.

Author Contributions: Conceptualization, J.-C.P.; methodology, Y.-S.S.; software, Y.-S.S.; validation, Y.-S.S.; formal analysis, Y.-S.S.; investigation, Y.-S.S. and S.-M.C.; resources, Y.-S.S.; data curation, Y.-S.S.; writing—original draft preparation, Y.-S.S.; writing—review and editing, J.-C.P.; visualization, Y.-S.S. and S.-M.C.; supervision, J.-C.P.; project administration, J.-C.P. All authors have read and agreed to the published version of the manuscript.

Funding: This research was a part of the project titled 'Development of Safety and Control Standards for Hydrogen Ships: Cargo Handling and Fuel Gas Supply Systems', funded by the Ministry of Oceans and Fisheries, Korea (20200456).

Institutional Review Board Statement: Not applicable.

Informed Consent Statement: Not applicable.

Data Availability Statement: Data are contained within the article.

Conflicts of Interest: The authors declare no conflicts of interest.

References

1. The International Energy Agency. *Energy Technology Perspectives*; The International Energy Agency: Paris, France, 2020.
2. International Maritime Organization. *Third IMO GHG Study*; International Maritime Organization: London, UK, 2020.
3. Ahmed, S.; Li, T.; Li, S.Y.; Chen, R. Comparative life cycle impact assessment of offshore support vessels powered by alternative fuels for sustainable offshore wind operations using machine learning. *J. Ocean Eng. Sci.* **2023**. [CrossRef]

4. International Chamber of Shipping. *Trade Policy Review*; International Chamber of Shipping: London, UK, 2022.
5. International Maritime Organization. *Revised GHG Reduction Strategy for Global Shipping Adopted*; International Maritime Organization: London, UK, 2023.
6. Song, H.C. Assessment of Cryogenic Material Properties of R-PUF Used in the CCS of an LNG Carrier. *J. Ocean Eng. Technol.* **2022**, *36*, 217–231. [CrossRef]
7. Aslannezhad, M.; Ali, M.; Kalantariasl, A.; Sayyafzadeh, M.; You, Z.; Iglauer, S.; Keshavarz, A. A review of hydrogen/rock/brine interaction: Implications for Hydrogen Geo-storage. *Prog. Energy Combust. Sci.* **2023**, *95*, 101066. [CrossRef]
8. Yang, N.; Deng, J.; Wang, C.; Bai, Z.; Qu, J. High pressure hydrogen leakage diffusion: Research progress. *Int. J. Hydrogen Energy* **2023**, *50*, 1029–1046. [CrossRef]
9. Pratt, J.W.; Klebanoff, L.E. *Optimization of Zero Emission Hydrogen Fuel Cell Ferry Design, with Comparisons to the SF-BREEZE (No. SAND2018-0421)*; Sandia National Laboratories: Albuquerque, NM, USA, 2018.
10. Bassam, A.M.; Phillips, A.B.; Turnock, S.R.; Wilson, P.A. An improved energy management strategy for a hybrid fuel cell/battery passenger vessel. *Int. J. Hydrogen Energy* **2016**, *41*, 22453–22464. [CrossRef]
11. Viking Cruises. Available online: https://www.vikingcruises.com/press/press-releases/2022-11-10-viking-takes-delivery-of-newest-ocean-ship.html (accessed on 18 October 2011).
12. Chung, S.M.; Seo, Y.S.; Jeon, G.M.; Kim, J.W.; Park, J.C. Parameter Study of Boiling Model for CFD Simulation of Multiphase-Thermal Flow in a pipe. *J. Ocean Eng. Technol.* **2021**, *35*, 50–58. [CrossRef]
13. Bartolomei, G.G.; Chanturiya, V.M. Experimental study of true void fraction when boiling subcooled water in vertical tubes. *J. Therm. Eng.* **1967**, *14*, 123–128.
14. Robinson, K. IC Engine Coolant Heat Transfer Studies. Ph.D. Thesis, University of Bath, Bath, UK, 2001.
15. Chung, S.M.; Jeon, G.M.; Park, J.C. Numerical approach to analyze fluid flow in a type C tank for liquefied hydrogen carrier (part 1: Sloshing flow). *Int. J. Hydrogen Energy* **2022**, *47*, 5609–5626. [CrossRef]
16. Krepper, E.; Koncar, B.; Egorov, Y. CFD modelling of subcooled boiling-concept, validation and application to fuel assembly design. *J. Nucl. Eng. Des.* **2007**, *237*, 716–731. [CrossRef]
17. Brraz Filho, F.A.; Caldeira, A.D.; Borges, E.M. A sensitivity analysis of the mass balance equation terms in subcooled flow boiling. In Proceedings of the International Nuclear Atlantic Conference (INAC), Recife, Brazil, 24–29 November 2013.
18. Gu, J.; Wang, Q.; Wu, Y.; Lyu, J.; Li, S.; Yao, W. Modeling of subcooled boiling by extending the RPI wall boiling model to ultra-high pressure conditions. *Appl. Therm. Eng.* **2017**, *124*, 571–584. [CrossRef]
19. Langari, M.; Yang, Z.; Dunne, J.F.; Jafari, S.; Pirault, J.P.; Long, C.A.; Thalackottore Jose, J. Conjugate heat transfer predictions for subcooled boiling flow in a horizontal channel using a volume-of-fluid framework. *J. Heat Transf.* **2018**, *140*, 104501. [CrossRef]
20. Ha, T.W.; Jeong, J.J.; Yun, B.J.; Yoon, H.Y. Improvement of the MARS subcooled boiling model for low-pressure, low-Pe flow conditions. *Ann. Nulcear Energy* **2018**, *120*, 236–245. [CrossRef]
21. Seo, Y.S.; Chung, S.M.; Park, J.C. Multiphase-thermal flow simulation in a straight vacuum-insulated LH2 pipe: Cargo handling system in LH2 carrier. *Ocean Eng.* **2024**, *297*, 117030. [CrossRef]
22. Fesmire, J.E. Standardization in cryogenic insulation systems testing and performance data. *Phys. Procedia* **2015**, *67*, 1089–1097. [CrossRef]
23. Lim, C.L.; Adam, N.M.; Ahmad, K.A. Cryogenic pipe flow simulation for liquid nitrogen with vacuum insulated pipe (VIP) and Polyurethane (PU) foam insulation under steady-state conditions. *Therm. Sci. Eng. Prog.* **2018**, *7*, 302–310. [CrossRef]
24. Kim, J.H.; Park, D.K.; Kim, T.J.; Seo, J.K. Thermal-Structural Characteristics of Multi-Layer Vacuum-Insulated Pipe for the Transfer of Cryogenic Liquid Hydrogen. *Metals* **2022**, *12*, 549. [CrossRef]
25. Rodi, W. Experience with Two-Layer Models Combining the k-e Model with a One-Equation Model Near the Wall. In Proceedings of the 29th Aerospace Sciences Meeting, Reno, NV, USA, 7–10 January 1991.
26. Menter, F.R. Two-Equation Eddy-Viscosity Turbulence Modeling for Engineering Applications. *AIAA J.* **1994**, *32*, 1598–1605. [CrossRef]
27. Wilcox, D.C. *Turbulence Modeling for CFD*, 3rd ed.; DCW Industries, Inc.: La Canada, CA, USA, 2006.
28. Kurul, N.; Podowski, M.Z. On the modeling of multidimensional effects in boiling channels. In Proceedings of the 27th National Heat Transfer Conference, Minneapolis, MN, USA, 28–31 July 1991; pp. 301–314.
29. Cole, R. A photographic study of pool boiling in the region of the critical heat flux. *AIChE J.* **1960**, *6*, 533–538. [CrossRef]
30. Lemmert, M.; Chawla, J.M. Influence of flow velocity on surface boiling heat transfer coefficient. *Heat Transf. Boil.* **1977**, *237*, 111–116.
31. Kocamustafaogullari, G.; Ishii, M. Interfacial area and nucleation site density in boiling systems. *Int. J. Heat Mass Transf.* **1983**, *26*, 1377–1387. [CrossRef]
32. Tolubinsky, V.I.; Kostanchuk, D.M. Vapour bubbles growth rate and heat transfer intensity at subcooled water boiling. In Proceedings of the 4th International Heat Transfer Conference, Paris, France, 31 August–5 September 1970. [CrossRef]
33. Rogers, J.T.; Li, J.H. Prediction of the Onset of Significant Void in Flow Boiling of Water. *J. Heat Transf.* **1994**, *116*, 1049–1053. [CrossRef]
34. International Association of Classification Societies. *LNG Bunkering Guidelines*; International Association of Classification Societies: London, UK, 2017.

35. Korean Register (KR). *Rules/Guidance for the Classification of Ships Using Low-Flashpoint Fuels*; Korean Register (KR): Busan, Republic of Korea, 2022.
36. DNV-GL. *Rules for Classification: Ships—DNVGL-RU-SHIP-Pt4Ch6 Piping Systems*; DNV-GL: London, UK, 2021.
37. Linstrom, P.J.; Mallard, W.G. *NIST Chemistry WebBook*; NIST Standard Reference Database Number 69; National Institute of Standards and Technology: Gaithersburg, MD, USA, 2020. [CrossRef]
38. Salama, A. Velocity Profile Representation for Fully Developed Turbulent Flows in Pipes: A Modified Power Law. *Fluids* **2021**, *6*, 369. [CrossRef]
39. Kays, W.M.; Crawford, M.E.; Weigand, B. *Convective Heat and Mass Transfer*, 4th ed.; McGraw-Hill Higher Education: Boston, MA, USA, 2005.
40. Fox, R.W.; McDonald, A.T.; Pritchard, P.J. Fluid Mechanics, Eighth Edition SI Version. Available online: https://www.amazon.co.uk/Fluid-Mechanics-8e-SI-Units/dp/9814720178 (accessed on 18 October 2011).
41. Monty, J.; Jones, M.; Chong, M. On the wall shear stress in fully developed turbulent channel flow. In Proceedings of the Tenth Asian Congress of Fluid Mechanics, Peradeniya, Sri Lanka, 17–21 May 2004.
42. Ghiaasiaan, S.M.; Chedester, R.C. Boiling incipience in microchannels. *Int. J. Heat Mass Transf.* **2002**, *45*, 4599–4606. [CrossRef]

Disclaimer/Publisher's Note: The statements, opinions and data contained in all publications are solely those of the individual author(s) and contributor(s) and not of MDPI and/or the editor(s). MDPI and/or the editor(s) disclaim responsibility for any injury to people or property resulting from any ideas, methods, instructions or products referred to in the content.